SCMNet: Toward Subsurface Chlorophyll Maxima Prediction Using Embeddings and Bi-GRU Network

Ao Wang ⃝, Baoxiang Huang ⃝, *Member, IEEE*, Jie Yang ⃝, Ge Chen ⃝, and Milena Radenkovic ⃝, *Member, IEEE*

Abstract—A subsurface chlorophyll maximum is an important ecological feature of planktonic ecosystems. Although the vertical profiles can be determined through the implementation of biogeochemical (BGC)-Argo buoy, this method is not compatible with the ocean observation requirements of high-resolution spatiotemporal measurements. Here, we demonstrate that deep learning can proficiently fill in these observational gaps when combined with sea surface data from ocean color radiometry. First, the sparse vertical profile data of BGC-Argo is fused with sea surface data to construct the benchmark dataset for deep learning. Second, encouraged by the idea of dense numerical representations, the comprehensive model combined with coupled embedding and bidirectional gated recurrent unit is proposed to inverse the vertical profile with BGC-Argo and satellite data. Then, the in-depth spatiotemporal analysis of the subsurface chlorophyll maxima phenomenon is performed by the parametric equation method and deep learning method as well. Finally, extensive experiments in the Northwest Pacific were conducted to demonstrate the effectiveness of the proposed methodology. The impressive results indicate that the proposed method can compensate for the lack of sparse in situ observations of chlorophyll concentration, the determination coefficient is increased by more than 20%. This study is of great significance to marine ecology and provides important insight into artificial intelligence in the study of subsurface oceanic phenomena.

Index Terms—Biogeochemical (BGC)-Argo, bidirectional gated recurrent unit (bi-GRU) network, deep embedding, remote sensing, subsurface chlorophyll maxima.

Ao Wang is with the Department of Computer Science and Technology, Qingdao University, Qingdao 266071, China (e-mail: w1032387902@126.com).

Baoxiang Huang is with the Department of Computer Science and Technology, Qingdao University, Qingdao 266071, China, and also with the Laboratory for Regional Oceanography and Numerical Modeling, Qingdao 266228, China (e-mail: hbx3726@163.com).

Jie Yang and Ge Chen are with the Laboratory for Regional Oceanography and Numerical Modeling, Qingdao 266228, China, and also with the School of Marine Technology, Institute for Advanced Ocean Study, Ocean University of China, Qingdao 266075, China (e-mail: yangjie2016@ouc.edu.cn; gechen@ouc.edu.cn).

Milena Radenkovic is with the School of Computer Science and Information Technology, The University of Nottingham, NG8 1BB Nottingham, U.K. (e-mail: milena.radenkovic@nottingham.ac.uk).

The dataset and Python code are available at GitHub DBAI to encourage competing methods.

Digital Object Identifier 10.1109/JSTARS.2023.3325922

I. Introduction

THE subsurface chlorophyll maximum (SCM) is an extensive interaction process [1] that contributes to the formation of sustained subsurface layers of elevated chlorophyll-a concentration (CHL) [2]. Our understanding of SCM phenomena has benefitted from in situ observations [3] while not enhanced with the increasing improvement of satellite observations [4] because measurements are limited to the superficial layer [5]. Considering the expensive in situ observations [6] and the high spatiotemporal resolution requirements of in-depth SCM study [7], the idea of filling the gap of in situ observations with sea surface data via regression method of machine learning has been formed.

In terms of observational data, a global network of biogeochemical sensors on Argo profiling floats (BGC-Argo) has accumulated data for more than ten years [8] and now can provide a high spatiotemporal dataset [9] of vertical profiles of CHL [10] that can be used to calculate three indicators of maximum, depth, and thickness of SCM phenomena [11]. Nevertheless, the vertical profiles data are still sparse [12] so cannot be conducive to reveal the nature of SCM and related dynamics mechanisms [13]. In the meantime, ocean remote sensing data have consistently provided intensive data [14] on the global ocean over the past few decades [15], with spatial resolutions ranging from meters to tens of kilometers [16]. Among them, CHL [17] and sea surface temperature (SST) [18] are recognized as essential variables [19] and are the primary parameters of ocean-color satellite products [20]. Naturally, the fusion of sea surface data to the vertical profile is competent for the data-intensive research paradigm of SCM phenomena.

With the rise of artificial intelligence [21], [22], machine learning has also infiltrated inversion methods with fused ocean surface information and ocean vertical profile structure [23]. An unsupervised neural network to retrieve ocean salinity patterns based on sea surface parameters is proposed and applied to physical surface measurements in the tropical Atlantic [24]. Further, a 3-D convolutional neural network is constructed to identify oceanic eddies using vertical structure [25]. In addition, artificial intelligence technology is also applied to reverse [26] and predict marine SCM [27]. Specifically, a shallow neural network with one hidden layer is trained to reconstruct the vertical structure of Mediterranean chlorophyll from in situ observational data and satellite remote sensing data [28], deep neural network with

a Gaussian radial basis activation function [29] is proposed to retrieve the vertical structure of CHL and calculate the associated SCM features based on ocean surface data [30]. Although these existing studies can extrapolate the intermediate ocean from sea surface data with efficient results, the dependence and mathematical continuity of ocean parameters on vertical depth, which is critical to ensure satisfactory results, has not been considered in the network design.

In order to solve this problem, some novel ideas and methods of neural network models applied in other fields can be used for reference. For example, in speech recognition tasks, the bidirectional gated recurrent unit (Bi-GRU) neural network first proposed by Schuster et al. [31] can provide more comprehensive sequence modeling capabilities and achieve better performance by simultaneously considering past and future context information. In addition, Liu et al. [32] proposed a multilabel classification model based on Bi-GRU that can simultaneously capture past and future contextual information, and proved the superior performance of the model in text classification through experiments on multilabel text classification tasks. In the prediction task, the method is also reflected. Fu et al. [33] proposed a prediction method of bearing service life based on deep Bi-GRU, mining the interdependence between mixed data and original data, which has good prediction accuracy and robustness. Inspired by the more comprehensive characteristics of Bi-GRU processing input information, the Bi-GRU is considered to be used in the modeling of ocean parameters to improve the accuracy of the model for vertical depth continuity prediction.

This article aims to explore data-driven and learning-based approaches to fill the gap of in situ observational data with dense surface-ocean data to facilitate extensive SCM research. The rest of this article is organized as follows. Section II formulates the problem and describes the related data. Section III illustrates the proposed method in detail. Section IV analyzes the inversion results of SCM profiles while presenting the indicators prediction results of different methods. Finally, Section V concludes this article.

II. PRELIMINARIES

A. Problem Formulations

The methodological approach taken in this study is regression and parameterization. Specifically, the prediction problem of SCM includes two parts. One is to regress the vertical profile with surface data, and the other is the parameterized process, which is to calculate three factors including maxima A, the depth D, and thickness 2σ. Let $\mathcal{X} = \{(\text{CHL}_i, \text{SST}_i, \text{lat}_i, \text{lon}_i, px_i)\}_{i=1}^{m}$ denote the vertical profile dataset with m profiles for SCM inversion, where m is the number of SCM vertical profiles, $\text{CHL}_i, \text{SST}_i \in \mathbb{R}$ is the corresponding sea surface data on the matching position $\text{lat}_i, \text{lon}_i$, $px_i = (px_{i1}, px_{i2} \ldots, px_{in}) \in \mathbb{R}$ is the i profile, where n is the depth of the profile. $y_i = (A_i, D_i, \sigma_i) \in \mathbb{R}$ is the ground truth of maxima A, the depth D, and thickness 2σ.

For the inversion problem, the input are the sea surface data $x_i :\to [\text{CHL}_i, \text{SST}_i, \text{lat}_i, \text{lon}_i]$ is the sea surface vector of the vertical profile px_i, the output are the vertical profile $y_i :\to px_i = (px_{i1}, px_{i2} \ldots, px_{in})$, the vertical profile

inversion process is the regression problem of deep learning. To assess the performance of the constructed method, the output value $f(x)$ of the network is expected to be infinitely close to the ground truth y, and the training objective of the inversion network is to achieve the minimum mean squared error, the detailed expression of the loss function can be formulated as follows:

$$\text{loss}_{\text{inversion}} = \sum_{px} \left[(f(x) - y)^2 \right] dx. \tag{1}$$

For the parameterized problem, the input $x_i :\to px_i = (px_{i1}, px_{i2} \ldots, px_{in})$, while the output is the SCM parameters $y_i :\to = [A_i; D_i; 2\sigma_i]$. Inspired by the Gaussian normal distribution model rotated by $90°$ in the study of the heat structure of the upper seawater [34], the complex mechanism of SCM formation is simplified as follows:

$$\text{CHL}(D) = A e^{-\frac{(D - D_{\max})}{2\sigma^2}}. \tag{2}$$

Correspondingly, the parameter A is the intensity of the SCM. The parameter D is the depth of the SCM. The parameter σ is the standard deviation, and 2σ means the thickness of the SCM.

B. Related Data

1) Sea Surface Chlorophyll Concentration: The CHL data products were generated by the ocean color component of the European Space Agency Climate Change Initiative project. In this study, the CHL dataset extended from 2017 to 2021 and had an eight-day temporal resolution and a 4KM spatial resolution.

2) Sea Surface Temperature: The daily SST dataset is the National Oceanic and Atmospheric Administration Optimum Interpolation SST product from Reynolds at $0.25°$ resolution. The dataset is interpolated to fill gaps on the grid and create a spatially comprehensive map of SST.

3) BGC-Argo Data: The vertical distribution of subsurface chlorophyll is obtained from BGC-Argo, which aims at developing a global network of BGC-Argo [35] and has obtained 113 465 chlorophyll profiles with a vertical measurement depth of 1000 m.

III. METHODOLOGIES

A. Data Preprocessing

This article collected 22 BGC-Argo profiling floats in the Northwest Pacific with a total of 2556 profiles at the depth of 300 m, as shown in Fig. 1. Considering the complexity of the occurrence and development of SCM, the research region is divided into three subregions: low latitude (10°N–25°N), middle latitude (25°N–35°N), and high latitude (35°N–55°N). The SCM dataset is built as follows. First, valuable information about the BGC-Argo profiles including the number, date, longitude (lon), latitude (lat), and concentration of chlorophyll are extracted. Second, the profile data are linearly interpolated with a resolution of 1 m. Then, a reasonable parameter range is determined according to the Gaussian model, thus the profiles without significant SCM features are filtered out. Finally, the satellite data and BGC-Argo data are matched spatially and temporally. The spatiotemporal matching of satellite data and BGC-Argo data includes two aspects of time and space. For each
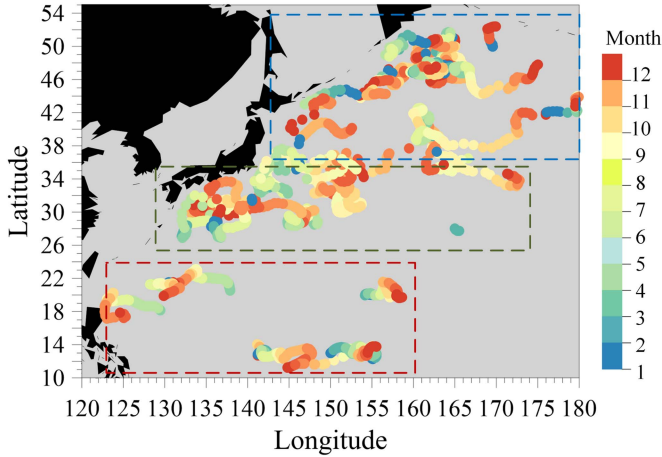
Fig. 1. Distribution of the 22 BGC-Argo floats required and the months measured. The three subregions are low latitude (red box), middle latitude (green box), and high latitude (blue box).
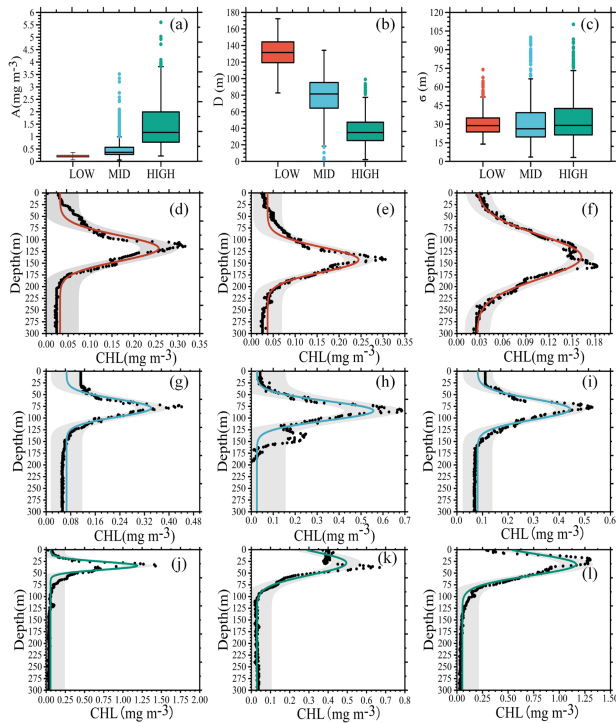

Fig. 2. Distribution of SCM dataset. (a)–(c) Range of parameters for the dataset. (d)–(f), (g)–(i), and (j)–(l) Three BGC-Argo profiles are chosen from different subregions randomly.

BGC-Argo observation profile data, on the one hand, it needs to match the remote sensing observation data corresponding to the time, that is, time matching. On the other hand, it needs to match the satellite data corresponding to its lon and lat, that is, spatial matching. Fig. 2(a)–(c) illustrates the overall parameter distribution of the SCM dataset. To intuitively demonstrate the availability of parameterized function (2), three BGC-Argo profiles, which are randomly selected in each subregion, are fitted as shown in Fig. 2(d)–(l). The dots represent the concentration values of chlorophyll in the vertical depth, which were obtained from the in situ data measured by BGC-Argo floats. The colored
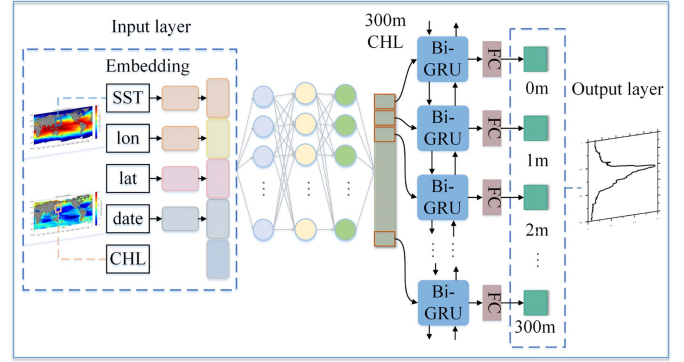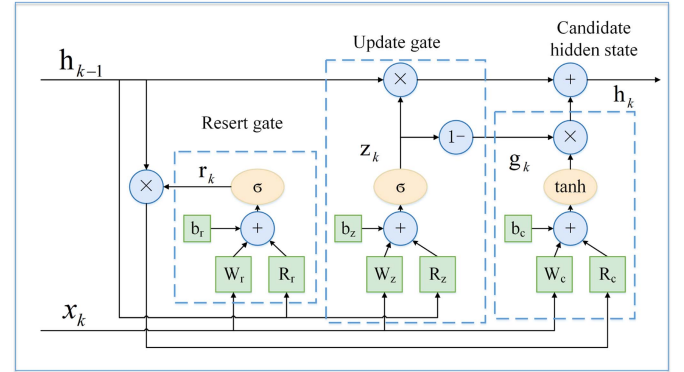
Fig. 3. Architecture of the proposed method.

curves represent the Gaussian curve fitted to the scattered points. The shaded part represents the 95% confidence interval of the fitted curve.

B. Overall Architecture of SCMNet

Moving on now to the inversion methods, SCM vertical distribution-oriented network named SCMNet is proposed based on coupled embedding and Bi-GRU frameworks, as illustrated in Fig. 3.

1) Embedding Module: To integrate a large number of basic features, the embedding module is adopted to digitally code SST, lon, lat, and date. Since the value of CHL is of strong floating-point type, it is directly concatenated with the encoded results.

2) Bi-GRU Cell Structure: Because the dependence of CHL data (the concentration value of the current depth is affected by the historical depth data, and the data of subsequent depths will also affect the concentration value of the current depth), the Bi-GRU module is employed to obtain more characteristic information from both positive and negative directions. At each depth, the data flow to two GRU modules in opposite directions at the same time, and the output sequence is determined by the two GRUs decided jointly.

The substructure GRU of Bi-GRU is shown in Fig. 3(b). The input of the GRU is the concentration value at the depth of k meters (x_k) and the hidden state at the depth of $k-1$ meters (h_{k-1}). The hidden state contains information about previous nodes at a specific depth. The output consists of the hidden nodes at the depth of k (y_k) and the hidden state at the depth of k, which

is passed to the next node. Its internal structure includes reset gate, update gate, and candidate hidden layer states. r_k is the reset gate at a depth of k meters, and it can be described in the following equation:

$$r_k = \sigma \left(W_r x_k + R_r h_{k-1} + b_r \right) \qquad (3)$$

where σ is the sigmoid activation function, x_k and h_{k-1} are the current input values, w_r and b_r are the weights and biases of the current input values, r_k determines how the new input information is combined with the previous memory. When r_k tends to 0, the model will discard the past hidden information, leaving only the current input information. When r_k tends to 1, it is considered that the hidden information in the past is useful, and it is added to the current information. z_k is the update gate at a depth of k meters, and it can be described in the following equation:

$$z_k = \sigma \left(W_z x_k + R_z h_{k-1} + b_z \right) \qquad (4)$$

where z_k determines the amount of previous depth data retained at the current depth. When z_k tends to 0, it means that there are more historical data forgotten. When z_k tends to 1, it means that there are more historical data to be passed on. The g_k is the state of the candidate hidden layer, and it can be described in the following equation:

$$g_k = \tanh \left(W_c x_k + R_c \left(r_k \times h_{k-1} \right) + b_c \right) \qquad (5)$$

where $r_k \times h_{k-1}$ indicates whether the past information is helpful to predict the concentration value of the next depth. The real hidden layer state formula is defined as follows:

$$h_k = z_k \times h_{k-1} + (1 - z_k) \times g_k. \qquad (6)$$

In the formula, $z_k \times h_{k-1}$ means selective forgetting of the original hidden state. $(1 - z_k) \times g_k$ represents the selective memory of the candidate's hidden state of the current node. The reverse GRU propagation process is the opposite. The calculation process of Bi-GRU is as the following:

$$\vec{h}_k = \text{GRU} \left(\vec{x}_k, \vec{h}_{k-1} \right) \qquad (7)$$

$$\overleftarrow{h}_k = \text{GRU} \left(\overleftarrow{x}_k, \overleftarrow{h}_{k-1} \right) \qquad (8)$$

$$h_k = f \left(\vec{W}_h \vec{h}_k + \overleftarrow{W}_h \overleftarrow{h}_k + b_k \right). \qquad (9)$$

IV. EXPERIMENTAL RESULTS

A. Implementations

The proposed SCMNet is constructed by Pytorch and trained on a computer with NVIDIA 2080ti and Windows system. The SCM dataset is divided into two parts: 80% of the data are training data and the remaining 20% are validation data. Basic statistical quantities used for the assessment of SCMNet performance concerning the observed values, including mean square error (MSE), root-mean-square error (RMSE), mean absolute error (MAE), and determination coefficient (R^2).

SCMNet is compared with multilayer perceptron (MLP), k-neighbors (KN), AdaBoost (AdaB), random forest (RF), and support vector regression (SVR) methods, and the results are

TABLE I
METRIC EVALUATION RESULTS OF SCM PARAMETERIZED BY SCMNET AND COMPARATIVE METHODS

A	Low				Mid				High			
Methods	SCMNet	MLP	KN	AdaB	SCMNet	MLP	KN	RF	SCMNet	MLP	KN	SVR
MSE	0.002	0.002	0.003	0.003	0.145	0.121	0.184	0.195	0.245	0.567	0.599	0.668
RMSE	0.048	0.050	0.049	0.049	0.381	0.348	0.429	0.442	0.495	0.753	0.774	0.853
MAE	0.037	0.041	0.043	0.038	0.189	0.178	0.166	0.155	0.335	0.497	0.501	0.516
R^2	0.235	0.062	0.164	-0.036	0.376	-0.793	0.328	0.139	0.743	-0.025	0.078	0.024

D	Low				Mid				High			
Methods	SCMNet	MLP	KN	AdaB	SCMNet	MLP	AdaB	SVR	SCMNet	MLP	KN	SVR
MSE	0.817	0.631	1.267	1.380	0.458	0.908	206.243	262.015	0.921	1.114	102.338	154.033
RMSE	0.904	0.794	1.125	1.174	0.677	0.952	14.361	16.186	0.959	1.055	10.116	12.411
MAE	0.581	0.628	0.643	0.777	0.514	0.616	11.222	12.258	0.587	0.608	7.325	8.780
R^2	0.183	0.368	-0.267	-0.380	0.541	0.092	-0.136	-1.619	0.079	-0.114	0.369	-1.054

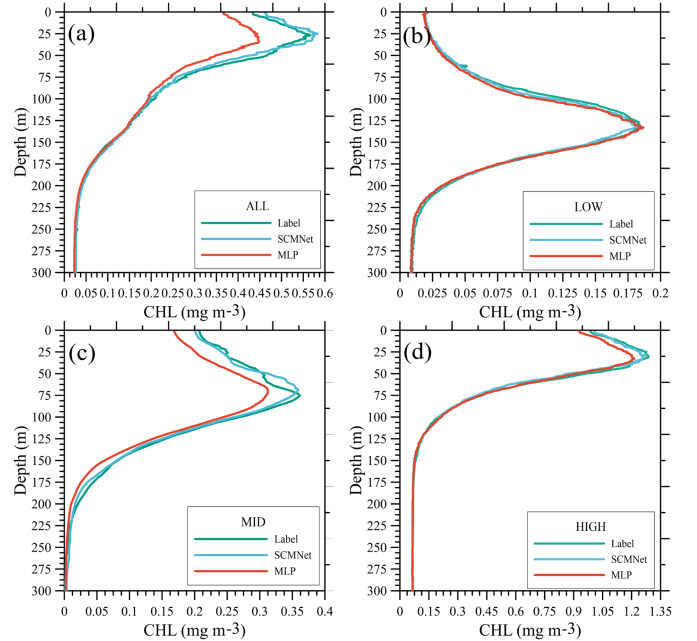| σ	Low				Mid				High			
Methods	SCMNet	MLP	KN	AdaB	SCMNet	MLP	XGB	KN	SCMNet	MLP	KN	SVR
MSE	0.629	0.933	0.668	0.869	0.741	1.092	96.716	113.004	0.729	1.005	118.370	138.918
RMSE	0.793	0.966	0.817	0.932	0.861	1.045	9.834	10.630	0.854	1.002	10.879	11.786
MAE	0.657	0.681	0.331	0.749	0.642	0.637	6.669	7.316	0.565	0.561	7.157	6.963
R^2	0.371	0.066	0.331	0.130	0.258	0.093	-0.047	-0.516	0.271	-0.005	-0.529	-0.828

Fig. 4. Inversion results of SCMNet and MLP models.

shown in Table I. It can be indicated that MLP is the most competitive method. Further, SCMNet and MLP are compared in more detail in the overall region and subregions. The output values for SCMNet and MLP are shown in Fig. 4. The R^2 value of SCMNet in the overall region is 0.8125, the R^2 value of MLP is 0.65, and the R^2 value has increased by 25%. And the R^2 of three subregions increased by about 21%, 24%, and 23%, respectively.

B. Ablation Experiments

In order to verify the improvement effect of embedding and Bi-GRU on the retrieval of chlorophyll concentration, ablation experiments are conducted on the embedding and Bi-GRU parts. Keep other parts of the model consistent, remove the embedding and Bi-GRU, and perform retrieval on the model. The evaluation results are shown in Table II. As can be seen from the table, all evaluation indicators are not as good as SCMNet. The results of the ablation experiments show that embedding and Bi-GRU

TABLE II
METRIC EVALUATION RESULTS OF THE ABLATION EXPERIMENTS BASED ON THE EMBEDDING AND BI-GRU MODULES IN THE OVERALL REGION AND THE THREE SUBREGIONS

Models	Regions	MSE	RMSE	MAE	R^2
SCMNet	All	0.0436	0.2089	0.0886	0.7492
	Low	0.0012	0.0355	0.0205	0.7789
	Mid	0.0276	0.1663	0.0703	0.7994
	High	0.0762	0.2762	0.1179	0.7537
Without Embeddings	All	0.1277	0.3573	0.1304	0.4432
	Low	0.0022	0.0474	0.0302	0.5880
	Mid	0.0608	0.2466	0.0972	0.5199
	High	0.1510	0.3886	0.1747	0.5123
Without Bi-GRU	All	0.0469	0.2167	0.0869	0.6224
	Low	0.0021	0.0467	0.0307	0.5990
	Mid	0.0280	0.1676	0.1072	0.5935
	High	0.1090	0.3627	0.2293	0.7332
Without Embeddings and Bi-GRU	All	0.1187	0.3445	0.2343	0.0459
	Low	0.0022	0.0479	0.0313	0.5797
	Mid	0.0601	0.2453	0.0967	0.1292
	High	0.1521	0.3901	0.1723	0.5087
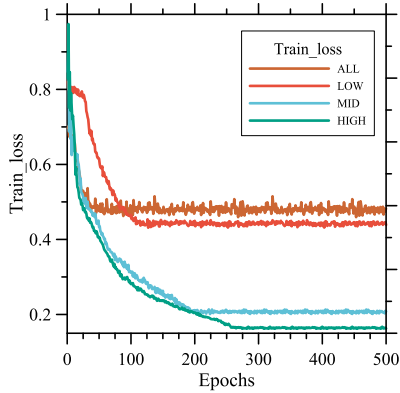
Fig. 5. Variation of loss values of the study region on the training set of 500 epochs.

Fig. 6. (a)–(d) Results of three subzones in different seasons. (e)–(g) Results of parameter in different latitudinal bands and different months.

play an important role in improving SCMNet model. Theirs existence have a positive impact which can significantly improve the performance of chlorophyll concentration retrieval, further verifying the effectiveness and necessity of embedding and Bi-GRU in this study.

C. Discussion of SCMNet Stability

During the training process, SCMNet performance is improved by iteratively adjusting SCMNet parameters to minimise the loss function. The loss curve of the SCMNet in the training process is plotted in Fig. 5 to intuitively evaluate the convergence and stability of the training process. It can be seen that in the overall region and the three subregions, the loss value of SCMNet gradually decreases and stabilizes during training. This indicates that SCMNet is effectively optimizing itself and improving its ability to fit the training data.

In order to evaluate the stability and generalization ability of the SCMNet, different datasets are used for training and testing the SCMNet, and the performance difference of the SCMNet on these datasets is observed. 5570 BGC-Argo observational profile data in the Mediterranean Sea are selected, and the dataset are constructed and are divided into training set and test set for experiments. The evaluation metrics MSE, RMSE, MAE, and
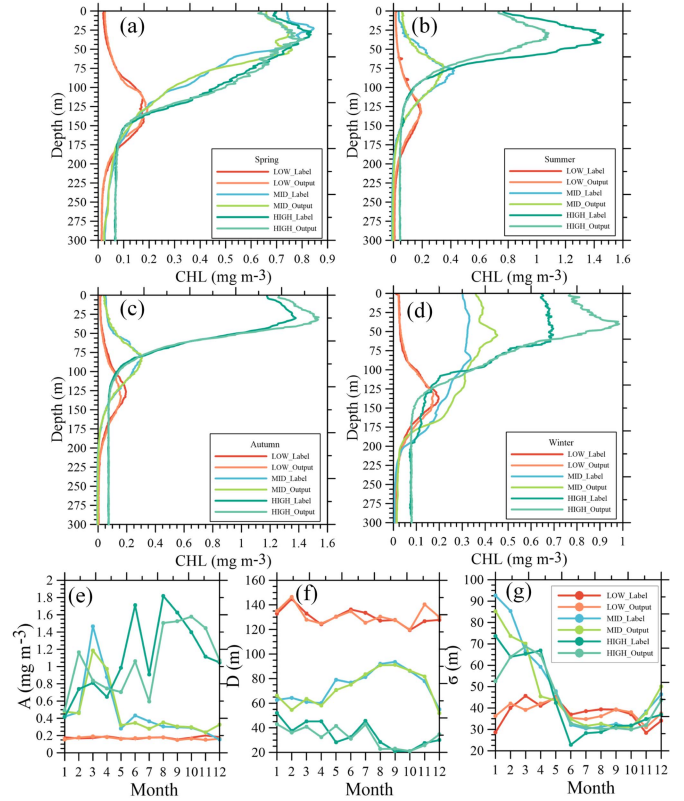
R^2 are 0.0083 $(\text{mg m}^{-3})^2$, 0.0916 mg m^{-3}, 0.0315 mg m^{-3}, 0.7593, respectively. There are consistent with the performance in the Northwest Pacific research region, indicating that SCMNet is able to effectively capture the characteristics and patterns of the data in different regions and make accurate predictions. This further enhances confidence in the performance of SCMNet.

D. SCM Spatial-Temporal Features

As can be seen from Fig. 4 that SCM presents different characteristics in different latitude bands. The intensity of SCM increases with the increase of the latitude zone, ranging from 0.18 mg m^{-3} in low latitudes to 0.35 mg m^{-3} in middle latitudes, and to 1.3 mg m^{-3} in high latitudes. The depth of SCM becomes shallower as the latitude zone increases, from 130 m in low latitudes to 30 m in high latitudes. There is no significant change in SCM thickness except for a slight decrease in the high-latitude region.

The seasonal characteristics of SCM at different latitudes are analyzed in more detail, as shown in Fig. 6(a)–(d). The fact that better predictions can be made throughout the year at lower latitudes has much to do with the uniform time distribution of SCM datasets at lower latitudes. In the middle and high latitudes, the in situ observations data themselves do not have obvious SCM characteristics in winter, which makes the winter prediction effect not good. Simultaneously, the prediction accuracy of intensity in high latitudes needs to be improved. In addition, the four seasons at low latitudes all present a nearly perfect "bell
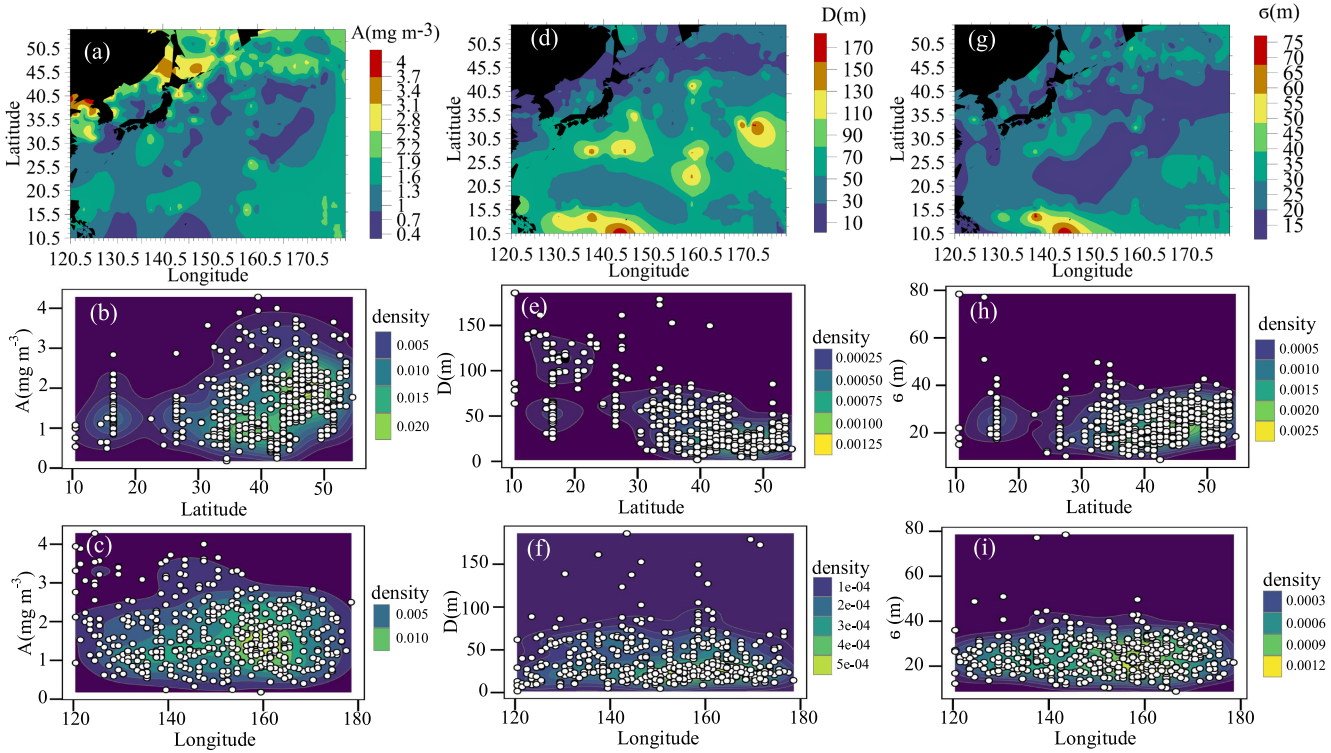
Fig. 7. Prediction results in the Northwest Pacific. (a)–(c), (d)–(f), and (g)–(i) are the prediction results and spatiotemporal decoupling analysis of parameters A, D, and σ, respectively.

shape," and the maximum value of the "bell shape" is around 0.2 mg m^{-3}. In spring, SCM in middle and high latitudes shows similar characteristics, which may be related to the similar SCM formation mechanism in coastal areas.

The profiles are also fitted according to the Gaussian function formula for the A, D, and σ parameters so as to understand the characteristics of the intensity, depth, and thickness of SCM in different latitudinal bands in different months, as shown in Fig. 6(e)–(g). For parameter A, the low-latitude region fluctuates very little in 12 months, concentrating on 0.2 mg m^{-3}, while the value of A in the middle-latitude region is relatively flat after June, corresponding to the profile shape of Fig. 6(b) and (c) in summer and autumn, which is close to a good "bell shape." The value of high latitude region A fluctuates greatly in 12 months. Although the accuracy of model prediction needs to be improved, there is roughly the same trend of change between the real value and the predicted value. For the parameter σ, there are slight differences with the latitude zone from January to May, and the value of σ is roughly the same after June. For parameter D, the model can achieve good prediction results each month, and it can be seen that the SCM depth varies significantly with different latitude zones. The depth of SCM at low latitudes is about 130 m, the average depth of SCM at middle latitudes is about 70 m, and the depth of SCM at high latitudes is about 30 m.

E. Case Study of Prediction Results

To further confirm the effectiveness of the proposed methodology, the date of 12 April 2019, which has the largest amount of profile data, is chosen as the case study. The detailed results of the prediction are shown in Fig. 7. The SCM intensity (A) is lower in low-latitude areas, and the higher the latitude, the greater the A value in high-density areas, and the concentration is around 2 mg m^{-3}, and the data fluctuate within a reasonable range. The SCM depth (D) becomes shallower as the latitude increases except for the accuracy of individual predictions that need to be improved, that is, the D value of the high-density area gradually decreases as the latitude increases. The SCM depth in the high-latitude area is concentrated at about 30 m, which is consistent with the SCM dataset. The σ value of SCM (the thickness is usually expressed by $2*\sigma$) is relatively concentrated and fluctuates between 0 and 40 m. Judging from different lon zones, the intensity, depth, and thickness of SCM are relatively concentrated, and there is no close relationship between their values and the height of lon zones. The predictions of the SCMNet model for the Northwest Pacific region are in high agreement with real in situ observations.

V. CONCLUSION

This article proposes an efficient methodology to inverse and parameterize the vertical structure of chlorophyll with sparse vertical profile data and sea surface data. The SCMNet model uses the data encoding method of coupled embedding and Bi-GRU to extract more features of satellite data and consider dependencies between depth sequences. The proposed method can achieve a more accurate prediction effect than KN, AdaB, RF, and SVR methods. Compared with the most competitive MLP method R^2 is improved by more than 20% in the study region and

three subregions. In order to evaluate the stability and generalization ability of the SCMNet, a series of experiments are conducted in selected Mediterranean areas. The evaluation metrics MSE, RMSE, MAE, and R^2 are 0.0083 $(mg/m^3)^2$, 0.0916 mg/m^3, 0.0315 mg/m^3, 0.7593, respectively. Spatiotemporal analysis of the SCM phenomenon is performed by combining the parametric equation method with the deep learning method as well. Meanwhile, the method is applied to the Northwest Pacific to verify its effectiveness and provides a new idea for studying the vertical marine ecological structure.

REFERENCES

[1] M. Cornec et al., "Deep chlorophyll maxima in the global ocean: Occurrences, drivers and characteristics," *Glob. Biogeochemical Cycles*, vol. 35, no. 4, 2021, Art. no. e2020GB006759.

[2] Z. Sun, S. Lu, and K. Omasa, "A new method to estimate the leaf chlorophyll content from multiangular measurements: Anisotropy index," *IEEE Trans. Geosci. Remote Sens.*, vol. 61, 2023, Art. no. 4401914.

[3] G. Anderson, "Subsurface chlorophyll maximum in the Northeast Pacific Ocean 1," *Limnol. Oceanogr.*, vol. 14, no. 3, pp. 386–391, 1969.

[4] R. Fablet, A. Chaigneau, and S. Bertrand, "Multiscale analysis of geometric planar deformations: Application to wild animal electronic tracking and satellite ocean observation data," *IEEE Trans. Geosci. Remote Sens.*, vol. 52, no. 6, pp. 3627–3636, Jun. 2014.

[5] J. P. Cannizzaro and K. L. Carder, "Estimating chlorophyll a concentrations from remote-sensing reflectance in optically shallow waters," *Remote Sens. Environ.*, vol. 101, no. 1, pp. 13–24, 2006.

[6] J. Su, C. Schallenberg, T. Rohr, P. G. Strutton, and H. E. Phillips, "New estimates of southern ocean annual net community production revealed by BGC-Argo floats," *Geophysical Res. Lett.*, vol. 49, no. 15, 2022, Art. no. e2021GL097372.

[7] C. Xu et al., "A modular remote sensing Big Data framework," *IEEE Trans. Geosci. Remote Sens.*, vol. 60, 2022, Art. no. 3000311.

[8] H. Claustre, K. S. Johnson, and Y. Takeshita, "Observing the global ocean with biogeochemical-Argo," *Annu. Rev. Mar. Sci.*, vol. 12, pp. 23–48, 2020.

[9] P. Chen, C. Jamet, and D. Liu, "LiDAR remote sensing for vertical distribution of seawater optical properties and chlorophyll-a from the East China Sea to the South China Sea," *IEEE Trans. Geosci. Remote Sens.*, vol. 60, 2022, Art. no. 4207321.

[10] A. Mignot, F. d'Ortenzio, V. Taillandier, G. Cossarini, and S. Salon, "Quantifying observational errors in biogeochemical-Argo oxygen, nitrate, and chlorophyll a concentrations," *Geophysical Res. Lett.*, vol. 46, no. 8, pp. 4330–4337, 2019.

[11] Y. Masuda et al., "Photoacclimation by phytoplankton determines the distribution of global subsurface chlorophyll maxima in the ocean," *Commun. Earth Environ.*, vol. 2, no. 1, 2021, Art. no. 128.

[12] A. S. Jutla, A. S. Akanda, and S. Islam, "Satellite remote sensing of space–time plankton variability in the Bay of Bengal: Connections to Cholera outbreaks," *Remote Sens. Environ.*, vol. 123, pp. 196–206, 2012.

[13] J. Su, P. G. Strutton, and C. Schallenberg, "The subsurface biological structure of Southern Ocean eddies revealed by BGC-Argo floats," *J. Mar. Syst.*, vol. 220, 2021, Art. no. 103569.

[14] C. E. Del Castillo and R. L. Miller, "On the use of ocean color remote sensing to measure the transport of dissolved organic carbon by the Mississippi River Plume," *Remote Sens. Environ.*, vol. 112, no. 3, pp. 836–844, 2008.

[15] L. Chen, C. Dong, and G. Wang, "GOCI-observed chlorophyll belts associated with sea-surface fronts in the East China sea," *IEEE Geosci. Remote Sens. Lett.*, vol. 17, no. 8, pp. 1299–1302, Aug. 2020.

[16] E. Pasetto, M. Riedel, F. Melgani, K. Michielsen, and G. Cavallaro, "Quantum SVR for chlorophyll concentration estimation in water with remote sensing," *IEEE Geosci. Remote Sens. Lett.*, vol. 19, 2022, Art. no. 1505705.

[17] D. J. Keith, "Satellite remote sensing of chlorophyll a in support of nutrient management in the Neuse and Tar-Pamlico River (North Carolina) estuaries," *Remote Sens. Environ.*, vol. 153, pp. 61–78, Oct. 2014.

[18] T. M. Chin, J. Vazquez-Cuervo, and E. M. Armstrong, "A multi-scale high-resolution analysis of global sea surface temperature," *Remote Sens. Environ.*, vol. 200, pp. 154–169, 2017.

[19] D. Shen, X. Li, L. Pietrafesa, and S. Bao, "Geostationary satellite observations and numerical simulation of typhoon-induced upwelling to the Northeast of Taiwan," in *Proc. IEEE Int. Geosci. Remote Sens. Symp.*, 2017, pp. 3552–3555.

[20] J. J. Cullen, "Subsurface chlorophyll maximum layers: Enduring enigma or mystery solved?," *Annu. Rev. Mar. Sci.*, vol. 7, no. 1, 2015, Art. no. 207.

[21] G. Song et al., "Surface UV-assisted retrieval of spatially continuous surface Ozone with high spatial transferability," *Remote Sens. Environ.*, vol. 274, 2022, Art. no. 112996.

[22] B. Huang, G. Chen, H. Zhang, G. Hou, and M. Radenkovic, "Instant deep sea debris detection for maneuverable underwater machines to build sustainable ocean using deep neural network," *Sci. Total Environ.*, vol. 878, 2023, Art. no. 162826.

[23] Q. Hu, X. Chen, Y. Bai, X. He, T. Li, and D. Pan, "Reconstruction of 3-D ocean chlorophyll a structure in the Northern Indian Ocean using satellite and BGC-Argo data," *IEEE Trans. Geosci. Remote Sens.*, vol. 61, 2023, Art. no. 4200513.

[24] M. B. Gueye, A. Niang, S. Arnault, S. Thiria, and M. Crépon, "Neural approach to inverting complex system: Application to ocean salinity profile estimation from surface parameters," *Comput. Geosci.*, vol. 72, pp. 201–209, 2014.

[25] B. Huang, L. Ge, X. Chen, and G. Chen, "Vertical structure-based classification of oceanic eddy using 3-D convolutional neural network," *IEEE Trans. Geosci. Remote Sens.*, vol. 60, 2022, Art. no. 4203614.

[26] S. Vadakke-Chanat and P. Shanmugam, "A model for the vertical chlorophyll-a distribution in the Bay of Bengal using remote sensing data," *IEEE Trans. Geosci. Remote Sens.*, vol. 58, no. 1, pp. 704–712, Jan. 2020.

[27] S. Kolluru and S. P. Tiwari, "Modeling ocean surface chlorophyll-a concentration from ocean color remote sensing reflectance in global waters using machine learning," *Sci. Total Environ.*, vol. 844, 2022, Art. no. 157191.

[28] M. Sammartino, S. Marullo, R. Santoleri, and M. Scardi, "Modelling the vertical distribution of phytoplankton biomass in the Mediterranean Sea from satellite data: A neural network approach," *Remote Sens.*, vol. 10, no. 10, 2018, Art. no. 1666.

[29] O. Gundogdu, E. Egrioglu, C. H. Aladag, and U. Yolcu, "Multiplicative neuron model artificial neural network based on Gaussian activation function," *Neural Comput. Appl.*, vol. 27, pp. 927–935, 2016.

[30] J. Chen et al., "Improved perceptron of subsurface chlorophyll maxima by a deep neural network: A case study with BGC-Argo float data in the Northwestern Pacific Ocean," *Remote Sens.*, vol. 14, no. 3, 2022, Art. no. 632.

[31] M. Schuster and K. K. Paliwal, "Bidirectional recurrent neural networks," *IEEE Trans. Signal Process.*, vol. 45, no. 11, pp. 2673–2681, Nov. 1997.

[32] H. Chen, G. Chen, P. Li, P. Zhao, and X. Wu, "Multi-label text classification via joint learning from label embedding and label correlation," *Neurocomputing*, vol. 460, pp. 385–398, 2021.

[33] B. Fu, W. Yuan, X. Cui, T. Yu, X. Zhao, and C. Li, "Correlation analysis and augmentation of samples for a bidirectional gate recurrent unit network for the remaining useful life prediction of bearings," *IEEE Sensors J.*, vol. 21, no. 6, pp. 7989–8001, Mar. 2021.

[34] M. R. Lewis, J. J. Cullen, and T. Platt, "Phytoplankton and thermal structure in the upper ocean: Consequences of nonuniformity in chlorophyll profile," *J. Geophysical Res., Oceans*, vol. 88, no. C4, pp. 2565–2570, 1983.

[35] C. Shu et al., "Biogeochemical model optimization by using satellite-derived phytoplankton functional type data and BGC-Argo observations in the Northern South China sea," *Remote Sens.*, vol. 14, no. 5, Mar. 2022, Art. no. 1297.